

Probing the quiet solar atmosphere from the photosphere to the corona

Ioannis Kontogiannis¹ · Costis Gontikakis¹ ·
Georgia Tsiropoula² · Kostas Tziotziou² ·

© Springer ●●●●

Abstract We investigate the morphology and temporal variability of a quiet Sun network region in different solar layers. The emission in several EUV spectral lines through both raster and slot time series, recorded by EIS/Hinode is studied along with H α observations and high resolution spectropolarimetric observations of the photospheric magnetic field. The photospheric magnetic field is extrapolated up to the corona showing a multitude of large and small scale structures. We show for the first time that the smallest magnetic structures both at the network and the internetwork contribute significantly to the emission in EUV lines, with temperatures ranging from $8 \cdot 10^4$ K to $6 \cdot 10^5$ K. Two components of transition region emission are present, one associated with small-scale loops that do not reach coronal temperatures and another one acting as an interface between coronal and chromospheric plasma. Both components are associated with persistent chromospheric structures. The temporal variability of the EUV intensity at the network region is also associated with chromospheric motions, pointing to a connection between transition region and chromospheric features. Intensity enhancements in the EUV transition region lines are preferentially produced by H α upflows. Examination of two individual chromospheric jets shows that their evolution is associated with intensity variations in transition region and coronal temperatures.

Keywords: Chromosphere, Quiet, Corona, Quiet, Transition Region

1. Introduction

The quiet solar atmosphere is highly variable in both space and time, due to the interaction between magnetic fields, solar differential rotation and convective

¹ Research Center for Astronomy and Applied Mathematics (RCAAM) Academy of Athens, 4 Soranou Efessiou Street, Athens, GR-11527, Greece email: jkonto@noa.gr

² Institute for Astronomy, Astrophysics, Space Applications and Remote Sensing, National Observatory of Athens, GR-15236, Penteli, Greece email: georgia@noa.gr email:

flows. At the solar surface, the large scale convective flows form a pattern of cells known as supergranular cells. The magnetic field lines are transported horizontally at the edges of the supergranular cells, resulting to the formation of the magnetic network, a web-like pattern, bright in strong resonance lines, such as Ca II H, that encompasses the slightly darker internetwork (IN). At the photosphere, the network consists of bright points that represent the cross-sections of magnetic flux tubes (Schrijver *et al.*, 1997). At the chromosphere, where the magnetic forces gain full control of the plasma dynamics, numerous elongated structures, seen in absorption in H α , stem from the network and cover part of the IN. These are traditionally called mottles (see Tsiropoula *et al.*, 2012, for a recent review) and are believed to outline the magnetic field of the chromosphere. The network pattern “survives” up to coronal temperatures (Gontikakis, Peter, and Dara, 2003; Tian *et al.*, 2008a,b), while at the corona, large scale closed magnetic loops and/or magnetic funnels dominate (Peter, 2001).

The transition region (TR), that lies between the hot and tenuous solar corona and the chromosphere, was modelled by Gabriel (1976), who took into account the magnetic field geometry resulting from the supergranular flows and the energy balance. In this model, the magnetic field flux tubes expand rapidly with height and form funnels that fill the TR and corona, while all energy necessary to maintain the TR was considered to be provided by heat conduction flowing downward from the corona. However, although this model gives consistent results for the differential emission measure (DEM) for temperatures higher than 10^5 K, it fails to explain the observed DEM at lower temperatures.

Dowdy, Rabin, and Moore (1986) suggested that small loops, confined within the network boundaries, with relatively low temperatures might contribute a significant amount to the lower TR emission. Since these loops are disconnected from the corona, they must be heated by an internal process. Feldman (1983) presented observational evidence that the TR plasma in the temperature range $4 \cdot 10^4$ – $2.2 \cdot 10^5$ K originates from the sum of unresolved, magnetically and thermally isolated structures, which he called “unresolved fine structures” (UFS). Spectroscopic observations bear signatures of the coexistence of loops with various sizes at the TR (Peter, 2001). In fact, a significant part of the magnetic flux of the network may be connected to nearby internetwork magnetic elements, forming low lying closed loops that surround the network (Schrijver and Title, 2003). Recent high resolution observations show that cool loop-like structures, thermally isolated from the corona, may exist in the TR quiet Sun network (Patsourakos, Gouttebroze, and Vourlidas, 2007; Vourlidas *et al.*, 2010). Hansteen *et al.* (2014) showed that small-scale structures (or the so-called UFS) are abundant in the TR, at least in lines formed at 10^5 K plasma, imaged by the Interface Region Imaging Spectrometer (IRIS) mission (De Pontieu *et al.*, 2014).

From a theoretical point of view, a mixture of small cool and intermediate-temperature loops with temperatures between 10^5 and 10^6 K could reproduce the observed emission in the lower TR (Sasso *et al.*, 2012; Sasso, Andretta, and Spadaro, 2015). State-of-the-art simulations (Guerreiro, Hansteen, and De Pontieu, 2013) show that the Si IV 1393 Å TR emission comes in fact from cool, low-lying loops. Schmit and De Pontieu (2016) came to the same conclusion

by combining IRIS observations and simulations. Their conclusions were partly based on detailed statistics between relatively low-resolution observations of the magnetic field (for QS standards) and radiance in the relatively cool (for TR standards) Si IV 1393 Å ($\log T = 4.9$) emission line. Therefore, studies that combine emission in both cool and hot emission lines can shed light to the existence of the different types of loops (in height and temperature). Even more, such studies, when combined with high resolution magnetograms can help us understand the magnetic connectivity between the different solar layers.

Regarding the temporal variability of the TR emission, until recently, localized broadenings of the TR spectral lines during short periods of time (explosive events; Brueckner and Bartoe, 1983) and intensity enhancements with lifetimes of the order of a few minutes (blinkers; Harrison, 1997; Bewsher *et al.*, 2003) were intensely studied. In retrospect, it is reasonable to assume that past resolution limitations permitted the detection only of the largest/brightest (in terms of spatial extent/intensity) of the TR variations. Indeed, higher spatial resolution observations of the TR revealed that small-scale, jet-like features are highly abundant (Tian *et al.*, 2014). It has also been found that small-scale chromospheric jets that exhibit rapid Doppler shift excursions (Roupe van der Voort *et al.*, 2009) are associated with plasma up to $8 \cdot 10^4$ K (Roupe van der Voort *et al.*, 2015), which is interpreted as a sign of their heating to TR temperatures. A statistical study by Henriques *et al.* (2016), showed that rapid chromospheric events are partly associated with low-corona (10^6 K) brightenings.

The possible association of chromospheric features with motions in the upper atmosphere is not new. It has been established that mottles and spicules carry more than enough mass to load the corona and the solar wind and that the major fraction of this flux returns back to the chromosphere (Tsiropoula and Tziotziou, 2004). In addition, these authors suggested that this returning flux could explain the persistent redshifts observed in the TR (Peter and Judge, 1999; Gontikakis and Dara, 2000; Tian *et al.*, 2010). The possible recycling of the solar plasma from the chromosphere to the corona and back has also been demonstrated with EUV spectroscopy (McIntosh and De Pontieu, 2009a,b).

In this study we address these issues using a unique dataset, which covers a remarkable range of atmospheric layers of a quiet solar region. We investigate the morphology and dynamics of different atmospheric layers/temperature regimes in relation to the magnetic field and explore the imprint of fine-scale chromospheric phenomena in the low-signal EUV measurements.

2. Data and Analysis

On October 15, 2007, several ground-based and space borne instruments were coordinated to observe the same quiet region located at the solar disk center (Figure 1). In this work we utilize data from that campaign, and more specifically those obtained with the *Solar Optical Telescope* and its Spectropolarimeter (SOT/SP Tsuneta *et al.*, 2008), the *EUV Imaging Spectrometer* (EIS; Culhane *et al.*, 2007) and the *X-Ray Telescope* (XRT; Golub *et al.*, 2007), onboard *Hinode*, the *Michelson Doppler Imager* (MDI; Scherrer *et al.*, 1995) onboard the *Solar*

Table 1. EIS Transition region and coronal spectral lines and XRT filter formation temperatures.

Spectral line/filter	T (K)
He II 256.32 Å	$10^{4.9}$
O V 192.80 Å	$10^{5.4}$
Fe VIII 185.21 Å	$10^{5.7}$
Mg VI 269.00 Å	$10^{5.7}$
Mg VI 270.40 Å	$10^{5.7}$
Mg VII 278.39 Å	$10^{5.8}$
Mg VII 280.75 Å	$10^{5.8}$
Si VII 275.35 Å	$10^{5.8}$
Fe XII 195.12 Å	$10^{6.2}$
“C_poly”	$10^{6.2}$

and Heliospheric Observatory (SoHO), as well as $H\alpha$ observations obtained with the ground-based *Dutch Open Telescope* (DOT; Rutten *et al.*, 2004).

MDI provided high-resolution magnetograms of the region between 08:00–11:00 UT (Figure 1, left panel). The cadence of the time series is 60 s and the spatial scale is $0.6''$. The SOT/SP performed two raster scans of the same area in the 6301.5 and 6302.5 Å Fe I lines at 09:05 and 09:15 UT. The field-of-view (FOV) of the raster scan (centered on the solar disk centre) was $50'' \times 164''$ and the spatial scale of the scans $0.32''$. The HAO/CSAC¹ team produced the corresponding photospheric vector magnetogram by performing the inversion of Stokes spectra via the MERLIN code. The line-of-sight (LOS) component of the magnetic field from MDI and SOT/SP was then used as an input to a current-free (potential) field extrapolation (Schmidt, 1964) to calculate the vector of the magnetic field up to 10 Mm. Further details on the inversion of the Stokes spectra and the comparison between MDI and SOT/SP data and extrapolated magnetic fields can be found in Kontogiannis, Tsiropoula, and Tziotziou (2011).

The EIS images plasma with upper chromosphere up to coronal temperatures. The EIS data include a series of $40''$ slot images, recorded between 08:14:40 and 09:40:15 UT with a 64 s cadence and a raster scan taken between 08:51–09:32 UT, with the $2''$ slit and 1 min exposure time. Out of the ten recorded spectral windows nine spectral lines were utilized, which are presented in Table 1, along with the corresponding ion formation temperature, taken from the CHIANTI database (v7.0).

Most of the available spectral lines are blended. These are either self-blends and/or lines with very high temperatures and very low intensities. For most of the lines, a single Gaussian was used to perform the fits. The Mg VII 280.75/278.39 Å and Mg VII 278.39 Å/Mg VI 269.00 Å line ratios are used to measure the electron

¹<http://www.csac.hao.ucar.edu/csac/dataHostSearch.jsp>

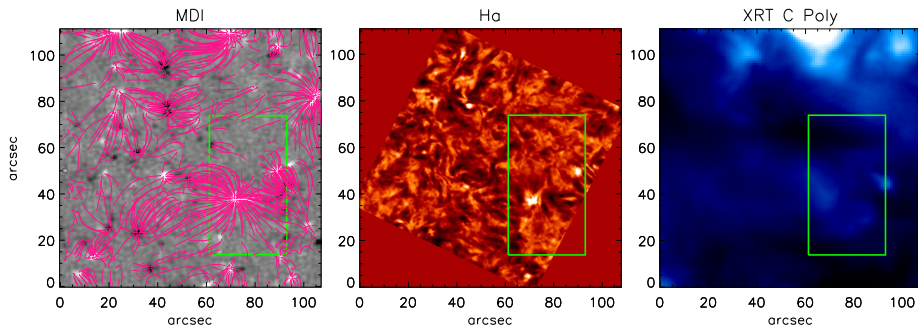


Figure 1. Temporally averaged images of a quiet Sun region at the disk center, obtained in October 15, 2007. From *left to right*: MDI magnetogram overlaid with the magnetic field lines, $H\alpha$ line center filtergram and XRT-“C_{poly}”. The *green* boxes indicate the common EIS and SOT/SP FOV.

density and temperature at the TR (Young *et al.*, 2007). The Ca XVII spectral line complex was treated following the method described by Levens *et al.* (2015), in order to calculate the intensity and velocity of the O V line. Given the unknown influence of blends in the width measurements, we only focus on the extracted peak intensity and velocity values.

The XRT provided time series of “C-poly” filtergrams of the solar disk center, with 25 s cadence and 1'' spatial scale (Figure 1, right panel). The temperature response of “C-Poly” peaks at $\log T = 6.2$. The acquisition time is not regular because the time series is often interrupted to obtain full-disk filtergrams. These filtergrams were removed and were not considered in the present analysis.

DOT observed the same region between 08:32–09:53 UT, providing speckle-reconstructed images in five positions along the $H\alpha$ profile (line centre, $\pm 0.35 \text{ \AA}$ and $\pm 0.70 \text{ \AA}$). The spatial scale of each image is 0.109 arcsec/pixel and the cadence is 30 s. Further details on preliminary reduction of the DOT observations can be found in Rutten *et al.* (2004). DOT data were rotated to match the FOV of the space-borne instruments (Figure 1, middle panel). Using the intensities at opposite positions $\Delta\lambda$ of the line profile at $\pm 0.70 \text{ \AA}$, the Doppler Signal (DS) was calculated at every pixel of the FOV through the formula:

$$DS = \frac{I(+\Delta\lambda) - I(-\Delta\lambda)}{I(+\Delta\lambda) + I(-\Delta\lambda)} . \quad (1)$$

and maps of DS were constructed. Positive (negative) DS denotes upward (downward) motion and is a qualitative representation of velocity (Tsiropoula, 2000).

The co-alignment of observations from different instruments, representing very different atmospheric regimes is usually a challenging procedure and requires a substantial amount of time and effort. First, we co-aligned the blue wing of $H\alpha$ with the co-temporal Ca II H images taken by the SOT (not used in this study) by matching the network bright points, visible in the blue wing of $H\alpha$ (Leenaarts *et al.*, 2006), with the ones in Ca II H and by using cross-correlation for fine-tuning the results. In a similar way, the MDI and SOT/SP magnetograms were co-aligned with $H\alpha$, while the SOT Ca II H image was co-aligned with the

co-temporal EIS He II slot images. The latter show the same network structure of the chromosphere but the boundaries are more extended. For this reason, the higher-resolution Ca II H images were first degraded to resemble the He II images. The XRT images were co-aligned with the Fe XII EIS slot images. Between the two wavelength ranges of EIS, there is a systematic offset (18'' and 1'' in the y- and x-direction, respectively) which was corrected by shifting the EIS short-wavelength windows. The EIS slot images were co-aligned with the raster intensity maps taken at the same wavelengths. We estimate that the common FOV is co-aligned with sub-arcsec accuracy.

3. Results

3.1. Quiet Sun structure from the photosphere to the corona

3.1.1. Morphology

In this section we infer the association between the emission in EUV channels, the underlying chromosphere and the overlying corona. We examine the spatial distribution of the emission/absorption in different wavelengths and compare it with the extrapolated chromospheric and coronal magnetic field.

Figure 1 provides the context of the observations by showing a region wider than the region-of-interest (ROI, marked by the green boxes, which outline the common FOV of all instruments). The MDI magnetogram at the left panel reveals the positive and negative magnetic patches that form the network. The field lines of the potential magnetic field are overplotted to show the connections between magnetic concentrations. These connections are also partly outlined by the dark elongated mottles (Tsiropoula *et al.*, 2012), seen in the H α line centre filtergram, in the middle panel of Figure 1. These low- β structures form the magnetic canopy (Kontogiannis *et al.*, 2010) and obscure most of the network boundaries (appearing bright in H α line wings) and IN. The XRT image (Figure 1, right panel) shows the overlying corona.

The positive polarity patch at $(x,y)\sim(70,35)$ is part of this network. It is simultaneously observed by all instruments and it is the focus of this study, along with its nearby IN. It connects to opposite polarity magnetic elements a) outside the green box, towards the left at $(x,y)\sim(50,45)$, via long magnetic field lines and b) inside the green box, towards the right, $(x,y)\sim(85,40)$, via short and low-lying magnetic field lines. The long magnetic field lines originate from the part of the network with the maximum magnetic flux density along the LOS, which, according to the SOT/SP magnetogram, reaches ~ 1.2 kG. The short, low-lying magnetic field lines are associated with closely packed H α absorption structures and appear darker in soft X-rays. The longer lines are partly outlined by radially distributed, elongated mottles and are associated with brighter coronal emission.

Figure 2 shows the ROI in more detail, as imaged by the EIS and SOT/SP rasters. For comparison we have also included a “synthetic” H α centre pseudo-raster, which was created as follows: after coaligning the H α and EIS FOV, the temporal information of each 2'' EIS slit exposure was used to select the closest,

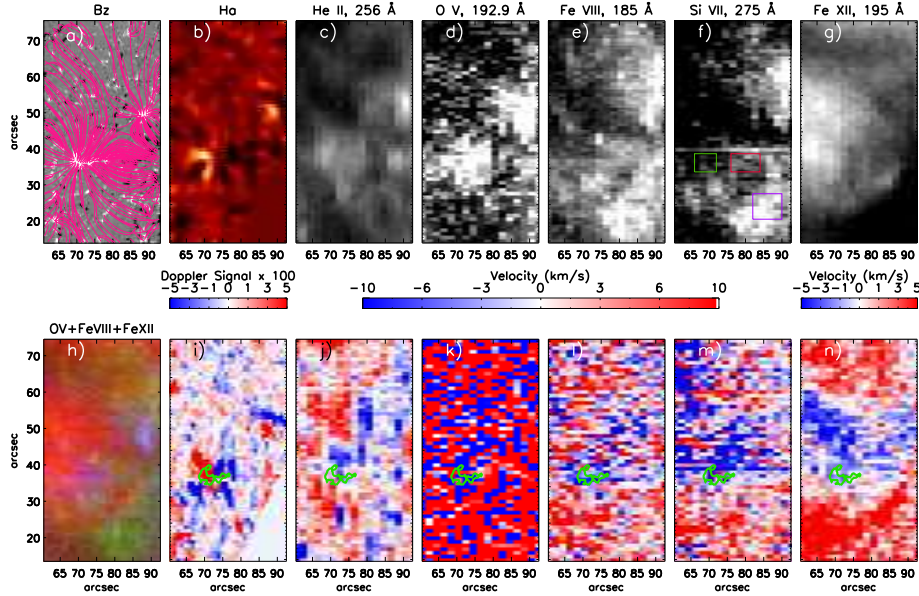


Figure 2. a) SOT/SP magnetogram with overlaid magnetic field lines, b) $H\alpha$ line centre intensity synthetic raster and c – g) peak intensities in He II 256.32 Å, O V 192.80 Å, Fe VIII 185.21 Å, Si VII 275.35 Å and Fe XII 195.12 Å, obtained from the EIS raster scans. The *rectangles* in the Si VII intensity map denote the areas where TR temperature and density were measured (see text). h) RGB image showing emission in O V (*blue*), Fe VIII (*green*) and Fe XII (*red*). i) $H\alpha$ DS \pm 0.70 Å synthetic raster, and j – n) Doppler velocities calculated from the EIS raster images of the *top* row. Here, *blue* (negative) corresponds to upward motion (towards the observer). The green contours mark the location of the network boundary. All images are cut-outs that correspond to the common FOV marked in Figure 1. The solar disk centre is located at $\sim(65,30)$.

in time, 2''-wide $H\alpha$ slice along the Y-axis. $H\alpha$ shows the magnetized plasma of the chromosphere, while a comparison with the extrapolated magnetic field of the SOT/SP magnetogram indicates that dark mottles largely outline the magnetic field lines that originate at strong magnetic flux concentrations.

Emission in the UV and EUV lines map the upper chromosphere, TR and corona. The He II and O V lines are associated with the network boundaries. The contrast between the network and the internetwork is lower in the He II line than in the O V line, in agreement with earlier observations (Judge and Pietarila, 2004). The higher temperature Fe VIII and Si VII lines (as well as Mg VI and Mg VII) exhibit a different morphology.

A comparison between the Fe VIII and Si VII emission and the extrapolated magnetic field shows that the TR plasma may be found either at the interface between the corona and the chromosphere, or in small scale low-lying loops, which do not reach coronal temperatures. From the following description, it will be evident, that these two “types” of transition region may be both associated

with the same network boundary, depending on the magnetic connectivity of the region.

The left part of the network, associated with the longest magnetic field lines, exhibits very weak emission in Fe VIII and Si VII and reaches coronal temperatures (as inferred by the intense emission in Fe XII). The right part of the network, associated with magnetic loops of various scales, shows intense emission in the Fe VIII and Si VII lines and weak or no coronal emission in Fe XII. These low-lying loops appear also as absorption features in H α . Intense emission in Fe VIII and Si VII accompanied by no coronal emission in Fe XII is also found at the lower part of the ROI, where the SOT/SP magnetogram shows numerous small scale magnetic concentrations with magnetic flux densities up to a few hundred Gauss.

Therefore, the EUV TR emission is not explicitly associated to the expansion of the magnetic field of the network. At the same network boundary and depending on the magnetic connectivity of the region, the TR plasma may be found either at the interface between the corona and the chromosphere or in small scale low-lying loops which do not reach coronal temperatures. This is also illustrated at the RGB image in Figure 2h. *Blue* represents the emission in O V and marks the location of the network while *red* is the overlying coronal emission of Fe XII. The areas in *green*, which represents Fe VIII, show us these two types of TR emission.

The first one, a “classical” TR, *i.e.* a thin boundary between the chromospheric and coronal plasma is located around the network and follows the expansion of the network magnetic field lines. There, the average electron temperature and density (Figure 2f, *green* rectangle) are equal to $5.74 \pm 0.08 \cdot 10^5 K$ and $3.6 \pm 0.5 \cdot 10^8 cm^{-3}$, correspondingly.

The second component, as already mentioned, is associated with magnetic flux tubes with very weak or no coronal counterpart at all. Some of them resemble the “intra-network” loops described by Dowdy (1993) and connect different parts of the network. These are seen at $(X,Y) \sim (80'', 38'')$. Others are associated with field lines that connect weak magnetic elements at the IN, reach heights lower than 1 Mm and can be as short as a few arcsec (lower right of the ROI). The Mg VII 278.39 Å/Mg VI 269.00 Å and Mg VII 280.75 Å/278.39 Å line ratios show us that the TR plasma in these small-scale loops is hotter and denser than the corresponding plasma found at the network. At the “intra-network” loops (Figure 2f, *red* rectangle) the corresponding values are $6.54 \pm 0.08 \cdot 10^5 K$ and $5.2 \pm 0.5 \cdot 10^8 cm^{-3}$ while at the low lying loops (Figure 2f, magenta rectangle) $6.37 \pm 0.08 \cdot 10^5 K$ and $4.4 \pm 0.4 \cdot 10^8 cm^{-3}$, respectively.

The He II velocity maps (Figure 2j) show some blueshifted features around the network. Some of these features coincide with (or appear to be the extensions of) areas with upward motions in H α , but there is no pixel-by-pixel correlation between velocities. The O V maps are very noisy and given the heavily blended line complex of the Ca XVII window, it is a question how trustworthy these velocity measurements are. The velocity maps of Fe VIII and Si VII are also very noisy, but they show that the network is dominated by upward motions, which agrees with previous studies of spectral lines at these temperatures (Kayshap, Banerjee, and Srivastava, 2015). In Fe XII, the bright coronal structure is clearly associated with upflows. Lacking observations of the other end of the structure

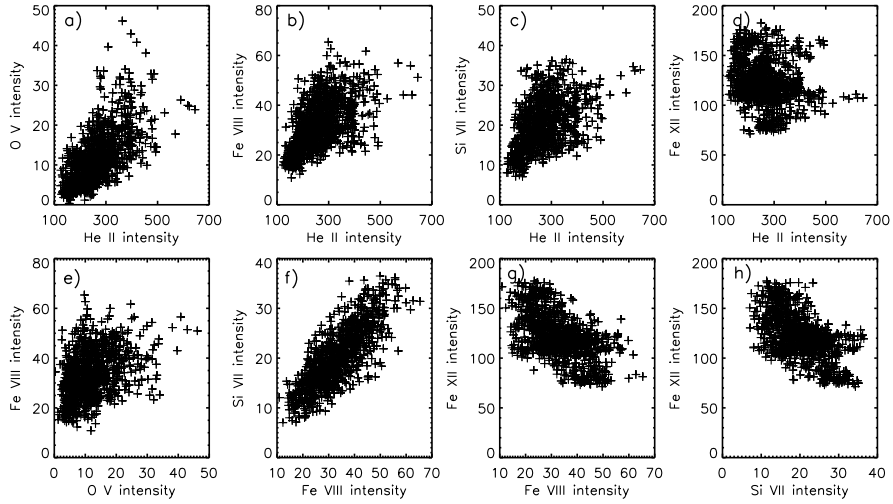


Figure 3. Scatter plots between the peak intensities of the EIS spectral lines of the rasters in Figure 2.

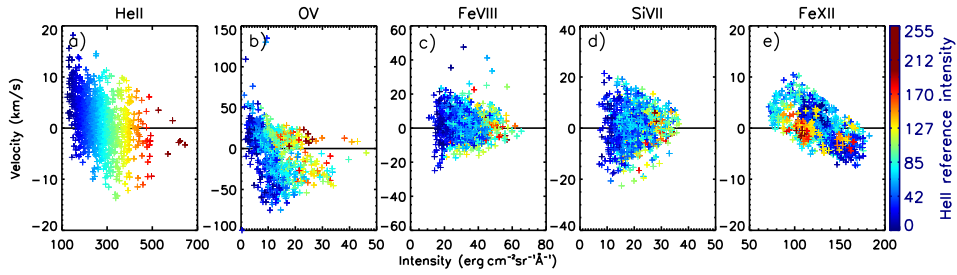


Figure 4. Velocity-Peak Intensity scatter plots for each of the spectral lines of the EIS raster in Figure 2. Different colors denote different He II peak intensity values, scaled to the 0-255 range.

(which is located outside the ROI), we cannot conclude on the specifics of this flow (*e.g.* if it is siphon flow or not).

3.1.2. Intensity - intensity and intensity - velocity correlations

The spatial structuring of the emission in different lines at the ROI as a function of temperature is also illustrated in the scatter plots of Figure 3, where the He II line intensity is used as a reference. The Pearson correlation coefficient between the peak intensity in the He II and the other TR lines drops as the temperature of the latter increases (0.64, 0.49, 0.41, and -0.11 for O V – He II, Fe VIII – He II, Si VII – He II and Fe XII – He II, respectively). The lack of correlation between Fe XII – He II shows that the coronal morphology of the network is altogether different from the chromospheric one. In Figure 3e–h, we present scat-

ter plots between peak intensities of different EIS lines. As expected, O V emission is weakly correlated with that of Fe VIII. This result shows how emission in the upper TR originates mostly from the small-scale loops and to a lesser degree from the network itself. The high correlation between Si VII – Fe VIII (0.8) indicates emission that comes from the same structures, while the moderate anticorrelation of these two lines with the coronal Fe XII line (-0.55 and -0.57, Figure 3g,h) shows that different parts of the network reach different temperatures.

In Figure 4 we plot the intensity-velocity relationship for the lines of the EIS raster shown in Figure 2. We use the He II intensity as a reference. Different He II (byte-scaled) intensity values are denoted with different colors and the transition from lower to higher He II intensity represents the transition from the IN towards the network. As the He II intensity increases, He II velocity values shift from being predominantly positive (downflows) to being predominantly negative (upflows). We should note that for the full raster the He II intensity-velocity scatter plot shifts from blue to red shifts, on average, for higher intensities, in accordance with other works (Brynildsen *et al.*, 1998). The O V line shows a similar transition but the velocity map is very noisy. A different velocity distribution arises at the upper TR lines (Fe VIII and Si VII), where velocities are roughly distributed symmetrically around zero. Above the network (corresponding to the highest He II intensity), we find mostly upward motions. At the corona (Fe XII line), the highest intensities are associated with blueshifts, which means that the bright coronal structures within the ROI is dominated by upward motions.

In summary, the dominant structure in the ROI is a large funnel-like magnetic structure, rooted at the left part of the network region and containing plasma heated up to coronal temperatures. At the base of this structure there is a “traditional” TR, *i.e.* a thin layer between the chromospheric and the coronal plasma. At the right part of the network, numerous shorter low-lying loops emanate, with various lengths down to a few arcsecs, which mostly contain plasma heated to upper TR temperatures and show no coronal emission. The funnel structure has $\sim 30\%$ lower electron density than the low-lying loops, while the latter reach temperatures up to $6 \cdot 10^5$ K. Furthermore, at a region outside the network, we find similar low-lying loops *i.e.* reaching $6 \cdot 10^5$ K and showing no coronal counterpart.

3.2. EUV brightness variations and relation to H α

We now turn to the analysis of the time-series of the slot images. In general, the slot images reveal the same morphology as Figure 2, but the corresponding features appear smoother since they are directly imaged and the EIS slot images mix spectral with spatial information. For this reason, the Fe VIII and Ca XVII windows (which contains the O V line) cannot be used.

In order to examine if there is any connection between the temporal variations at the chromosphere, TR and corona, we constructed the maps of standard deviation (“SDEV” hereafter) of the 40" slot intensities, H α line center intensities and the DS at $\pm 0.70 \text{ \AA}$ from line center (Figure 5).

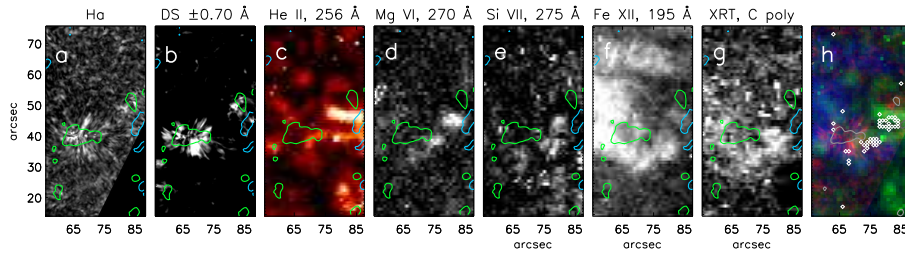


Figure 5. a–g) Standard deviation maps derived from the EIS slot time-series for the ROI. As a reference, *green* (*blue*) contours represent cotermporal positive (negative) magnetic flux density derived from the MDI magnetograms. h) RGB image showing DS ± 0.70 Å (*red*), He II (*green*) and Fe XII (*blue*) standard deviation. Diamonds mark higher than 2σ Mg VI variations while the grey contour outlines the magnetic footpoints of the network.

High SDEV patches are found in all maps mostly around the magnetic field of the network. In the H α intensity and DS maps (panels a–b), these patches are elongated and are associated to the chromospheric motions along the magnetic field lines while at the He II, Mg VI and Si VII these are more roundish as per the lower spatial resolution of EIS. Also, the lower EIS sensitivity in the upper transition region emission (Young *et al.*, 2007) results to lower SDEV values and fewer patches. In the Fe XII line and the XRT soft X-ray emission, high SDEV is found inside the bright coronal structure, around the network. We note that the temporal variations inside these patches are, in most cases, spatially coherent, showing that they are the result of a physical process and not noise. Most prominent is the elongated bright feature at $(x, y) \sim (80, 45)$, visible in the He II, Mg VI and, to a lesser extent, in Si VII. This patch corresponds to a continuous increase of EUV emission, due to a small scale emerging dipole.

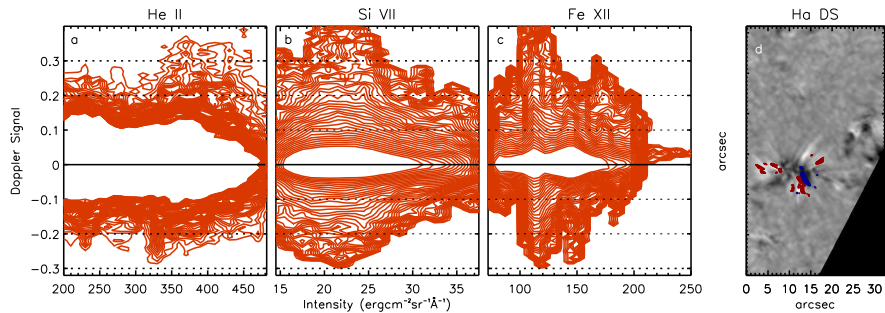


Figure 6. a–c) Scatter plots between H α DS ± 0.70 Å and He II, Si VII and Fe XII intensities, respectively. For better comparison, *horizontal lines* mark some DS values. Positive DS values denote upward motions. The density of points is plotted as *contours* for better visibility. d) Average DS ± 0.70 Å map. Overplotted with *red* are the locations where DS was higher than 0.3, and EUV intensities were simultaneously in the ranges 340–460 for He II, 19–26 for Si VII and 100–140 for Fe XII. Similarly, in *blue* we mark the locations where DS was lower than -0.2, and EUV intensities were simultaneously in the ranges 300–350 for He II, 15–28 for Si VII and 100–130 for Fe XII

The spatial distribution of high SDEV in all channels denotes the impact of the small scale events of the network region on the TR and the fanning-out of

the magnetic field lines with height. We have plotted an RGB image containing information from all atmospheric layers in Figure 5h to illustrate this. Many He II high SDEV patches (in *green*) appear adjacent to or as extensions of the ones in H α DS (in *red*) while the coronal SDEV patches (in *blue*) are located further outwards. For many of these features, there is also detectable temporal variation in the Mg VI and Si VII emission (*white diamonds*). From the overall appearance of the RGB image in Figure 5h, we conclude that at least part of the emission variations in EIS windows, from the photosphere up to the corona, is related to the fine structures observed at the chromosphere. Although the resolution of EIS does not allow the detection of fine structures at the TR, as *e.g.* in Hansteen *et al.* (2014), our results confirm that in many cases, features at higher temperatures appear as extensions of chromospheric ones (Pereira *et al.*, 2014). Through these EIS observations, this finding is now extended to higher TR and coronal temperatures.

By visual comparison of the He II and H α filtergrams, it may be coarsely implied that absorption features in H α appear in emission in He II. The enhanced emission of the helium lines has lead researchers to propose alternative formation mechanisms for this line (see *e.g.* Judge and Pietarila, 2004, for a comprehensive review). Based on observations of He I and He II lines by SUMER and CDS, these authors suggest that the mixing of neutral helium with the coronal plasma, above the magnetic canopy, increases the emission in these lines. These ions can be advected either along or across the magnetic field and neutrals can be excited by the hot electrons found at higher atmospheric layers. As a result, the helium emission is overall enhanced and the contrast between network and internetwork regions is reduced. It is possible that macroscopic motions of chromospheric features, *e.g.* spicules, may play a role in this process. It should be noted that Andretta *et al.* (2000) have found an anti-correlation between the H α red wing and He II intensities, while Golding, Leenaarts, and Carlsson (2017), showed that the enhanced He II emission is caused primarily by non-equilibrium helium ionization effects.

The effect of chromospheric motions along the magnetic field on the He II emission can be inferred by the preceding description of the SDEV maps. High SDEV patches in He II are the extensions of the corresponding chromospheric ones around the network (see Figure 5a, b and c). To further investigate the effect of chromospheric motions on the He II emission we plot, in Figure 6a, the He II emission *versus* the H α DS at $\pm 0.70 \text{ \AA}$ from line center, for each pixel and time step. The distribution is largely symmetric, on top of which lie excursions of higher positive and negative DS. Highest positive values of the H α DS at $\pm 0.70 \text{ \AA}$ (which correspond to upward chromospheric motion) are associated with He II intensities higher than $340 \text{ erg cm}^{-2} \text{ sr}^{-1} \text{ \AA}^{-1}$. Some of the downward motions also appear to be associated with enhanced He II emission, but to a less extent. Taking into account that large DS at $\pm 0.70 \text{ \AA}$ may correspond to relatively higher Doppler shifts of the H α profile, we conclude that the He II intensity is affected by those H α events with the highest velocities.

We also examine whether there is an association between chromospheric motions and the emission in Si VII and Fe XII slot data (Figure 6b and 6c). For Si VII, higher positive and negative DS produce emission enhancements up to

$28 \text{ erg cm}^{-2} \text{ sr}^{-1} \text{ \AA}^{-1}$. The effect of high positive and negative DS is also evident on coronal intensities. Overall, while upward motions produce highest emission in He II, the corresponding motions only contribute to low and intermediate emission in Si VII and Fe XII. The locations where high H α DS (>0.3) appear simultaneously with the corresponding intensity EUV enhancements were calculated. These are marked with red on the time-averaged DS map in Figure 6d and are indeed located along features that exhibit persistent upward motion. Similarly, we over-plotted the enhancements that correspond to high negative H α DS (<-0.2). These are found along a persistently red-shifted feature on the network. Taking into account projection effects (due to the slanted orientation of the small scale structures) which hinder a pixel by pixel comparison, the results shown in Figure 6 indicate that enhancements in the low/intermediate intensity range of upper atmospheric emission are mostly associated with upward chromospheric motions.

3.3. Chromospheric jets and EUV emission

Regardless of the relatively low resolution of EIS, the He II slot time-series reveals pronounced activity around the network. We present two examples of jets observed clearly in the He II slots, that are related to H α jet-like features and result to conspicuous variations at the overlying layers.

In Figure 7 we present a TR brightening at $(x, y) \sim (75, 30)$, associated with a chromospheric jet (elongated white structure in H α DS at $\pm 0.70 \text{ \AA}$, third row). The increase in the He II intensity (note that the brightest features appear dark in the EUV emission in Figure 7) is co-spatial with the upward moving jet and increased absorption from a bundle of mottles in the H α (second and third row). The H α jet has already started to evolve and the bright blob appears 1 min later in He II protruding from the network. Its expansion follows the evolution of the chromospheric jet. In He II it starts as a roundish brightening and evolves into a bifurcating jet-like feature. In the next frame, a brightening also appears along the network, adjacent to the origin of the first blob. In H α there is a bundle of mottles that exhibit intense upward motion. This upward moving chromospheric material has a similar bifurcated shape and, owing to the higher spatial resolution of DOT, we may discern several mottles that comprise the jet. The morphology of the feature in H α and He II is indicative of a three-dimensional structure seen at different heights. The jet is followed by downward chromospheric motions and then it fades from view in the He II window. At the hotter Si VII window, no corresponding feature is detected, but there are variations in brightness, located further out from the jet. The Fe XII slots show no elongated or blob-like features. However, related variations in intensity can be found in the x-t diagram (Figure 8a, red contour) constructed along the structure (green line in Figure 7). The upward motion of the material corresponds to increased emission in both He II and Fe XII. Concerning the latter, this increase cannot be discerned against the overlying coronal emission in the images but is visible in the x-t diagram. Increased emission is detected at the Mg VI line which is co-spatial with the downflows in H α that follow the upward motion.

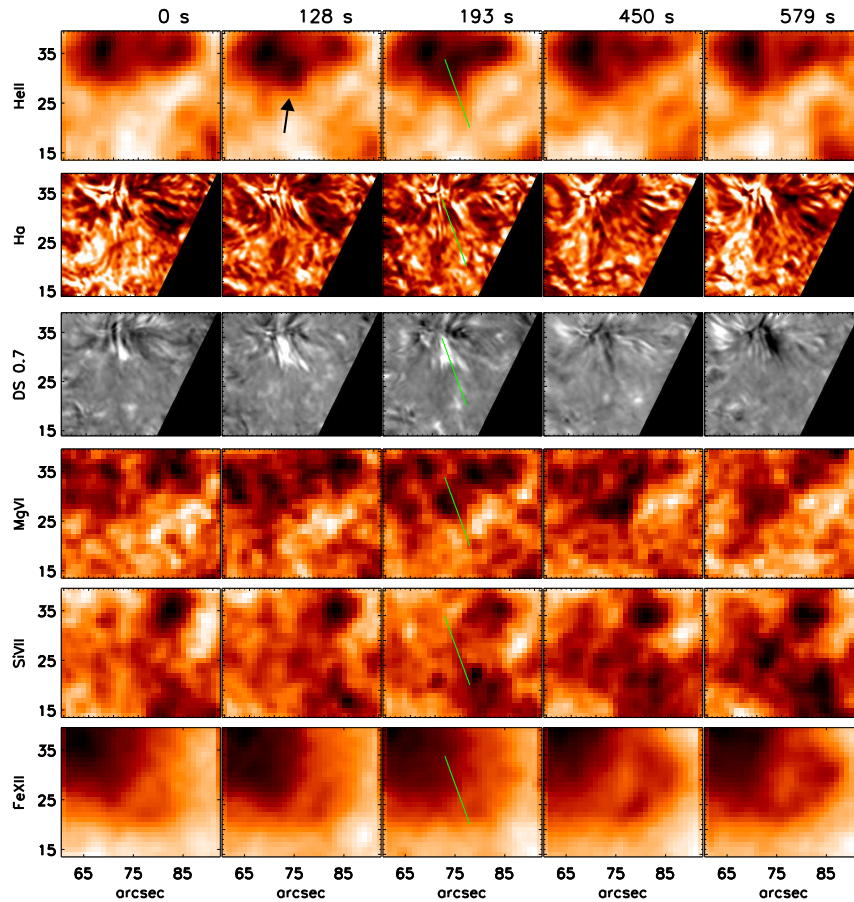


Figure 7. The evolution of an He II brightening, which is cospatial with a chromospheric jet in $H\alpha$. Left column, from *top to bottom*: snapshots of He II intensity, $H\alpha$ centre intensity and $H\alpha$ DS at $\pm 0.70 \text{ \AA}$, Mg VI, Si VII and Fe XII. The EUV windows have been multiplied by a gaussian kernel and the color table has been inverted, for better visibility. The *black arrow* at the top row indicates the position of the brightening in He II. The *green lines* indicate the position where a slice was taken for the x-t diagram, shown in Figure 8.

The lightcurves in Figure 8 were calculated by summing the signal along the entire slice (Figure 8) for each time instance. It is worth noting that the event starts with upward motion of material seen in absorption in $H\alpha$. Its duration is about 7 min during which, the intensity in He II increases, following closely the DS curve (Figure 8c). This evolution confirms the relation between He II emission and upward chromospheric motion described in Sec. 3.2. Soft X-ray and Fe XII emission (Figure 8e) both follow the DS curve very closely, demonstrating a coronal response to this jet. The rest of the TR lines also exhibit a small peak during the upward motion of the jet. Judging by the

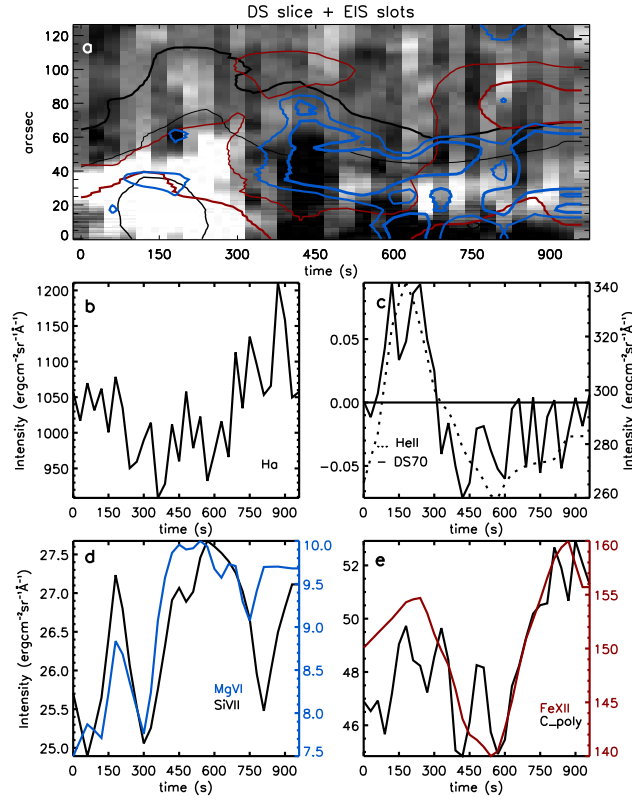


Figure 8. a) X-t diagram of the H α DS at $\pm 0.70 \text{ \AA}$, along the slice marked with the *green* line in Figure 7, with over-plotted contours of He II (black), Fe XII (red) and Mg VI (blue). Thicker contours stand for more intense emission. b-e) summed intensities along the slices taken in *different lines* (and H α $\pm 0.7 \text{ \AA}$ DS).

H α DS curve, the material then descends and the intensity in He II decreases. During this downward chromospheric motion, the intensity of the upper TR lines (Mg VI and Si VII) increases notably (see the blue contour in Figure 8a and d). This evolution suggests a connection between the chromospheric motion of material and emission up to the corona. Interestingly, the bulk of the TR emission during this event, is associated with the downflow. Madjarska and Doyle (2003) describe a similar (although larger) event which initiates as upflow and then becomes predominantly downflow, in the N v 1238 \AA line, while in Nelson and Doyle (2013), a chromospheric jet exhibits signatures in the EUV channels up to the corona. It is possible that this TR brightening is associated with a macrospicule seen on disk (Madjarska *et al.*, 2006).

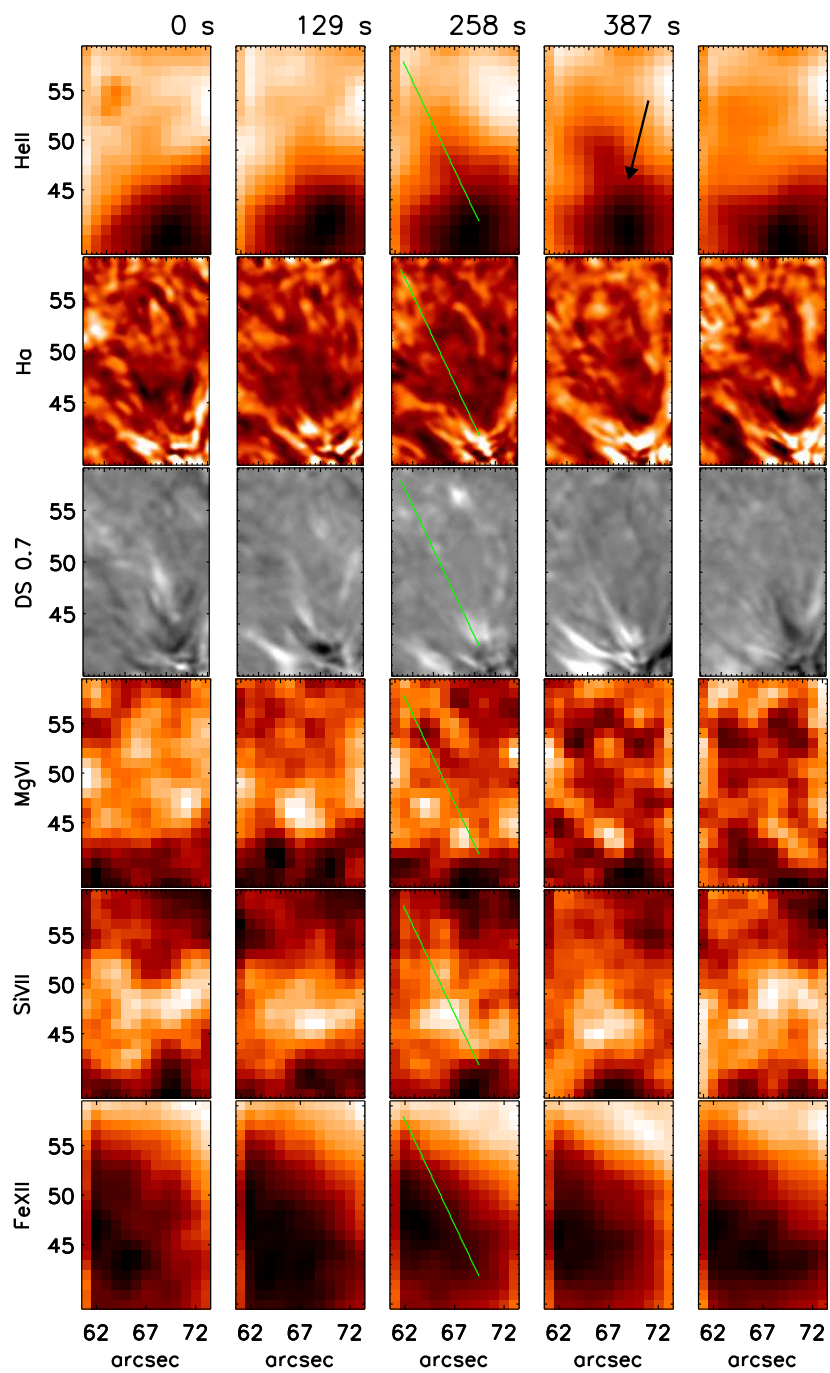


Figure 9. Same as Figure 7 but for another jet-like feature.

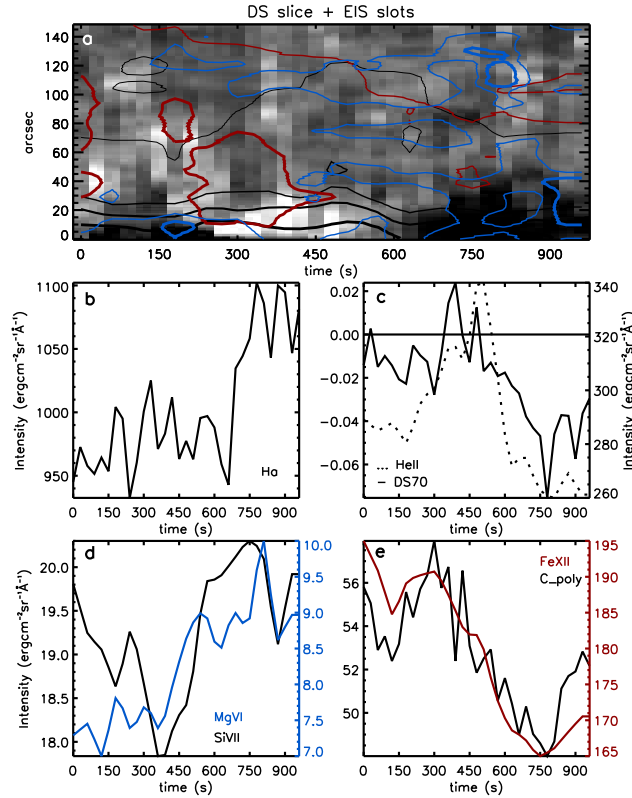


Figure 10. Same as Figure 8 but for the feature of Figure 9.

The evolution of the jet in Figure 7 suggests that the downflow of spicular (mottle) material could be the generator of TR region brightenings at the network (see *e.g.* Gallagher *et al.*, 1999; Bewsher *et al.*, 2003). The upper chromospheric (He II) and coronal (Fe XII) emission are both co-temporal with the upward motion of the chromospheric material while the bulk of the TR emission follows a few minutes later, during the downflow of the material (negative $\text{H}\alpha$ DS). Unfortunately, due to lack of spectral information for the TR lines, we do not know whether the emission in Mg VI and Si VII is accompanied by redshifts in these lines. Based on these observations, the origin of the high temperature component of the chromospheric jet, whose cooling seems to produce the subsequent increase in lower temperatures (TR lines) can only be conjectured.

Another example of a TR jet associated with a chromospheric feature is shown in Figure 9. This is more pronounced in the He II emission. The $\text{H}\alpha$ shows thin features with upward motion but shorter than the He II feature. The DS maps (Figure 9) and x-t slice map (Figure 10) show that at the footpoints of the jet,

located at $(x, y) \sim (70, 43)$, there is clear upward motion (Figure 9, third row, third panel), preceded by a bi-directional flow (Figure 9, third row, second panel). In $H\alpha$ mottles, these flows have been associated with heating and are attributed to reconnection (Tsiropoula and Tziotziou, 2004). The He II counterpart is more extended than the $H\alpha$ feature and the $H\alpha$ absorption (seen also as lower intensity at Figure 10b) is more intense near the footpoints. If a reconnection process is indeed producing this feature, then it is reasonable to expect that the plasma is heated, moving away from the formation temperature of $H\alpha$ absorption and producing the peaks in He II, Fe XII and soft X-rays. These peaks are roughly co-temporal with the upward chromospheric motions at $t \sim 350$ s (Figure 10c and e). Then, emission at the TR lines starts to increase (Figure 10d), after $t \sim 450$ s, when the coronal emission decreases and the chromospheric motion is downward, suggesting a further evolution similar to the previous case.

If the observed bi-directional flow is attributed to a reconnection process, then a significant mass content can be driven towards upper atmospheric layers as suggested by Tsiropoula and Tziotziou (2004). Unfortunately, the low resolution MDI data are not adequate to support this scenario. On the other hand, the high resolution SOT/SP data show that small scale magnetic fields are abundant at the IN so the interaction of small scale magnetic structures with the opposite polarity magnetic fields of the network provides support to a magnetic reconnection process as a realistic scenario.

4. Conclusions and discussion

In this work we use multi-wavelength observations of a quiet Sun region at the solar disk center, covering all atmospheric layers from the photosphere up to the corona. The observations consist of simultaneous $H\alpha$ line profile observations from DOT, TR and low corona observations from EIS/Hinode (both raster images with important spectral information and time-series of slot images) and soft X-ray filtergrams from XRT/Hinode combined with magnetic field observations from MDI/SoHO and SOT/SP/Hinode. We exploit this unique dataset in order to examine the morphology, dynamics, temporal variability and relation to the magnetic field of the observed region, as well as the connectivity and interplay between the different atmospheric layers.

As it is already stated (see *e.g.* Tian *et al.*, 2010) the magnetic structure of the transition region and corona and their connectivity with the chromosphere and photosphere are not completely understood. Utilizing extrapolations of the observed magnetic field together with EUV observations we were able to show that along with the “traditional” TR, which acts as an interface between chromospheric and coronal plasma, significant emission in the TR temperatures comes from small-scale magnetic structures. These may be either part of the network or formed by the abundant small-scale magnetic fields of the IN. Their sizes are up to a few arcseconds, while signs of their emission at temperatures from $8 \cdot 10^4$ K to $6 \cdot 10^5$ K are found. This is a very important finding because it shows that numerous small-scale cool and of intermediate temperatures, low-lying loops are contributing to the TR emission. These results agree with the

TR model of Dowdy, Rabin, and Moore (1986) and the description of Peter (2001) and Schrijver and Title (2003). TR emission is mostly attributed to low-lying loops, but also associated with phenomena near the footpoints of coronal structures corroborating thus the results presented in Patsourakos, Gouttebroze, and Vourlidas (2007) and Tian *et al.* (2010).

Recent high resolution observations have shown that small-scale loops are abundant in EUV emission in temperatures near 10^5 K (Guerreiro, Hansteen, and De Pontieu, 2013; Hansteen *et al.*, 2014; Schmit and De Pontieu, 2016) but no comparison with high resolution magnetograms was made in these analyses. Small scale loops have been reported in active region plages in Barczynski, Peter, and Savage (2017), but their association with magnetic fields was not feasible due to the low resolution of the HMI magnetogram. The difficulty in quiet Sun is that the omnipresent small scale magnetic structures evade detection in low resolution magnetograms. Therefore, although it is reasonable to associate TR emission with the footpoints of coronal structures, the confirmed existence of small scale photospheric elements (Lites *et al.*, 2008) inevitably leads to the presence of short scale magnetic loops that connect the network boundaries with the IN, in a manner similar to what is described *e.g.* in Schrijver and Title (2003). It is also reasonable to expect that numerous small scale magnetic loops will permeate the internetwork. The high resolution SOT/SP magnetogram and the calculated magnetic field lines in Figure 2 now justify this assumption, since small-scale magnetic elements are abundant in the FOV and are connected with short field lines. As seen at the lower right of the panels in Figure 2, these small-scale structures are associated with emission up to the Si VII formation temperature and very weak or no coronal emission.

Previous studies have utilized co-temporal EUV wide-slit observations by CDS and have shown that there is a correspondence between chromospheric and coronal temporal variations (Ugarte-Urra *et al.*, 2004). Here, we extend these studies by examining simultaneous high resolution chromospheric $H\alpha$ observations along with higher resolution TR and coronal observations for the first time. We showed that upper TR emission variations are located mostly around the network and appear as extensions of or co-spatially with the underlying chromospheric variations. The SDEV maps of Figure 5 allow the conjecture that chromospheric mottles may reach temperatures at least up to $6 \cdot 10^5$ K. It has already been shown that some chromospheric features appear more extended in higher TR temperatures observed by IRIS (Pereira *et al.*, 2014). We extend this finding to even higher TR temperatures, in the spectral lines observed by EIS.

Two individual jets related to the network and stand out clearly in $H\alpha$ observations were studied. It was found that brightenings in the TR and corona may be the result of typical chromospheric motions, not necessarily the fastest ones. In these events, the bulk of the TR emission at the vicinity of the funnel-like structure is associated with the downflows that follow. We were also able to examine, for the first time, the impact of chromospheric motions, as derived through the $H\alpha$ Doppler signals (a far more reliable measure of chromospheric motions than the intensity on one position on the $H\alpha$ profile used in some studies), on the transition region and coronal emission recorded with the slot images of EIS. The highest chromospheric DS seem to be related to increased emission in TR

temperatures. In the case of He II, the highest emission is associated with large H α blueshifts, but it is relatively unaffected by redshifts, justifying a velocity redistribution mechanism (MacPherson and Jordan, 1999; Andretta *et al.*, 2000). In the case of Si VII and Fe XII emission, we find an association between Doppler-shifted chromospheric events and low-to-intermediate EUV intensities. These associations are found along persistent upward-moving chromospheric features. It is quite interesting that not necessarily the fastest events (which are usually the focus of other studies), but rather typical network structures are associated with these intensity enhancements.

Recent high resolution observations have shown that highly Doppler-shifted events appear at the chromosphere in very short time-scales (Roupe van der Voort *et al.*, 2009). So far, the difference in the resolution achieved by instruments that provide chromospheric and upper TR/coronal observations has not facilitated easy comparison between features at different atmospheric heights and temperature regimes. To overcome this difficulty, McIntosh and De Pontieu (2009b) have studied line asymmetries in EUV spectra, concluding that they point to a heating mechanism during rapidly-changing chromospheric events. In the recent works of Roupe van der Voort *et al.* (2015) and Henriques *et al.* (2016), it is shown that, indeed, rapidly-changing chromospheric events are associated with brightenings up to coronal temperatures. In addition, observations in plages and coronal holes near the limb have shown that these rapidly-changing events are associated with coronal heating (De Pontieu *et al.*, 2011). Although there is an ongoing debate on whether these events may indeed produce heating (see *e.g.* Klimchuk, 2012; Klimchuk and Bradshaw, 2014), our analysis contributes to the existing (and increasing) literature in a twofold manner: 1) by showing that there is an EUV counterpart of Doppler-shifted chromospheric features at the upper TR and coronal temperature emission, even at the quiet solar conditions and 2) that not necessarily the fastest of these events are associated with this emission. These findings were deduced from a very quiet region, at the solar disk center with no criterion on the H α DS imposed on the observations; besides, the spatial, temporal and spectral resolution of DOT does not allow for the detection of very fast moving features at the chromosphere. If indeed these events are related with rapid variations in EUV temperatures, then, arguably, the low temporal-spatial resolution of EIS smears them out and they appear as low magnitude intensity enhancements.

Our results demonstrate the potential of observations like the ones provided by the EIS instrument. The ability to record emission in several spectral windows, although at the expense of spectral resolution, is invaluable, because it can provide simultaneous overview of plasmas at different temperatures, especially when combined with high resolution magnetograms and chromospheric observations. Of course, the chromospheric events described in Sec. 3.3 are of small scale. However, the corresponding signals in the EUV, although extremely weak, are conspicuous. This is an indication that TR is highly variable even at the smallest scales and we believe that a combination of high quality images and spectral observations will shed light on the relations between chromospheric fine structures, TR transients, and coronal emission.

Acknowledgements The authors would like to thank the anonymous referee whose valuable comments greatly improved the manuscript. The observations have been funded by the Optical Infrared Coordination network (OPTICON, <http://www.ing.iac.es/opticon>), a major international collaboration supported by the Research Infrastructures Program of the European Commission's sixth Framework Program. The research was partly funded through the project "SOLAR-4068", which is implemented under the "ARISTEIA II" Action of the operational program "Education and Lifelong Learning" and is cofunded by the European Social Fund (ESF) and Greek national funds. The DOT was operated at the Spanish Observatorio del Roque de los Muchachos of the Instituto de Astrofísica de Canarias. The authors thank P. Sütterlin for the DOT observations and R. Rutten for the data reduction. Hinode is a Japanese mission developed and launched by ISAS/JAXA, collaborating with NAOJ as a domestic partner, and NASA and STFC (UK) as international partners. Scientific operation of the Hinode mission is conducted by the Hinode science team organized at ISAS/JAXA. This team mainly consists of scientists from institutes in the partner countries. Support for the post-launch operation is provided by JAXA and NAOJ (Japan), STFC (U.K.), NASA, ESA, and NSC (Norway). Hinode SOT/SP Inversions were conducted at NCAR under the framework of the Community Spectro-polarimetric Analysis Center (CSAC; <http://www.csac.hao.ucar.edu>). The authors would like to thank Dr S.H. Park for valuable help in the magnetic field extrapolation.

References

- Andretta, V., Jordan, S.D., Brosius, J.W., Davila, J.M., Thomas, R.J., Behring, W.E., Thompson, W.T., Garcia, A.: 2000, The Role of Velocity Redistribution in Enhancing the Intensity of the HE II 304 Å Line in the Quiet-Sun Spectrum. *ApJ* **535**, 438. DOI. ADS.
- Barczynski, K., Peter, H., Savage, S.L.: 2017, Miniature loops in the solar corona. *A&A* **599**, A137. DOI. ADS.
- Bewsher, D., Parnell, C.E., Pike, C.D., Harrison, R.A.: 2003, Dynamics of Blinkers. *Sol. Phys.* **215**, 217. DOI. ADS.
- Brueckner, G.E., Bartoe, J.-D.F.: 1983, Observations of high-energy jets in the corona above the quiet sun, the heating of the corona, and the acceleration of the solar wind. *ApJ* **272**, 329. DOI. ADS.
- Brynildsen, N., Brekke, P., Fredvik, T., Haugan, S.V.H., Kjeldseth-Moe, O., Maltby, P., Harrison, R.A., Wilhelm, K.: 1998, SOHO Observations of the Connection Between Line Profile Parameters in Active and Quiet Regions and the Net Red Shift in EUV Emission Lines. *Sol. Phys.* **181**, 23. DOI. ADS.
- Culhane, J.L., Harra, L.K., James, A.M., Al-Janabi, K., Bradley, L.J., Chaudry, R.A., Rees, K., Tandy, J.A., Thomas, P., Whillock, M.C.R., Winter, B., Doschek, G.A., Korendyke, C.M., Brown, C.M., Myers, S., Mariska, J., Seely, J., Lang, J., Kent, B.J., Shaughnessy, B.M., Young, P.R., Simnett, G.M., Castelli, C.M., Mahmoud, S., Mapson-Menard, H., Probyn, B.J., Thomas, R.J., Davila, J., Dere, K., Windt, D., Shea, J., Hagood, R., Moye, R., Hara, H., Watanabe, T., Matsuzaki, K., Kosugi, T., Hansteen, V., Wikstol, Ø.: 2007, The EUV Imaging Spectrometer for Hinode. *Sol. Phys.* **243**, 19. DOI. ADS.
- De Pontieu, B., McIntosh, S.W., Carlsson, M., Hansteen, V.H., Tarbell, T.D., Boerner, P., Martinez-Sykora, J., Schrijver, C.J., Title, A.M.: 2011, The Origins of Hot Plasma in the Solar Corona. *Science* **331**, 55. DOI. ADS.

- De Pontieu, B., Title, A.M., Lemen, J.R., Kushner, G.D., Akin, D.J., Allard, B., Berger, T., Boerner, P., Cheung, M., Chou, C., Drake, J.F., Duncan, D.W., Freeland, S., Heyman, G.F., Hoffman, C., Hurlburt, N.E., Lindgren, R.W., Mathur, D., Rehse, R., Sabolish, D., Seguin, R., Schrijver, C.J., Tarbell, T.D., Wülser, J.-P., Wolfson, C.J., Yanari, C., Mudge, J., Nguyen-Phuc, N., Timmons, R., van Bezooijen, R., Weingrod, I., Brookner, R., Butcher, G., Dougherty, B., Eder, J., Knagenhjelm, V., Larsen, S., Mansir, D., Phan, L., Boyle, P., Cheimets, P.N., DeLuca, E.E., Golub, L., Gates, R., Hertz, E., McKillop, S., Park, S., Perry, T., Podgorski, W.A., Reeves, K., Saar, S., Testa, P., Tian, H., Weber, M., Dunn, C., Eccles, S., Jaeggli, S.A., Kankelborg, C.C., Mashburn, K., Pust, N., Springer, L., Carvalho, R., Kleint, L., Marmie, J., Mazmanian, E., Pereira, T.M.D., Sawyer, S., Strong, J., Worden, S.P., Carlsson, M., Hansteen, V.H., Leenaarts, J., Wiesmann, M., Aloise, J., Chu, K.-C., Bush, R.I., Scherrer, P.H., Brekke, P., Martinez-Sykora, J., Lites, B.W., McIntosh, S.W., Uitenbroek, H., Okamoto, T.J., Gummin, M.A., Auker, G., Jerram, P., Pool, P., Waltham, N.: 2014, The Interface Region Imaging Spectrograph (IRIS). *Sol. Phys.* **289**, 2733. DOI. ADS.
- Dowdy, J.F. Jr.: 1993, Observational evidence for hotter transition region loops within the supergranular network. *ApJ* **411**, 406. DOI. ADS.
- Dowdy, J.F. Jr., Rabin, D., Moore, R.L.: 1986, On the magnetic structure of the quiet transition region. *Sol. Phys.* **105**, 35. DOI. ADS.
- Feldman, U.: 1983, On the unresolved fine structures of the solar atmosphere in the 30,000-200,000 K temperature region. *ApJ* **275**, 367. DOI. ADS.
- Gabriel, A.H.: 1976, A magnetic model of the solar transition region. *Philosophical Transactions of the Royal Society of London Series A* **281**, 339. DOI. ADS.
- Gallagher, P.T., Phillips, K.J.H., Harra-Murnion, L.K., Baudin, F., Keenan, F.P.: 1999, Transient events in the EUV transition region and chromosphere. *A&A* **348**, 251. ADS.
- Golding, T.P., Leenaarts, J., Carlsson, M.: 2017, Formation of the helium extreme-UV resonance lines. *A&A* **597**, A102. DOI. ADS.
- Golub, L., DeLuca, E., Austin, G., Bookbinder, J., Caldwell, D., Cheimets, P., Cirtain, J., Cosmo, M., Reid, P., Sette, A., Weber, M., Sakao, T., Kano, R., Shibasaki, K., Hara, H., Tsuneta, S., Kumagai, K., Tamura, T., Shimojo, M., McCracken, J., Carpenter, J., Haight, H., Siler, R., Wright, E., Tucker, J., Rutledge, H., Barbera, M., Peres, G., Varisco, S.: 2007, The X-Ray Telescope (XRT) for the Hinode Mission. *Sol. Phys.* **243**, 63. DOI. ADS.
- Gontikakis, C., Dara, H.C.: 2000, Dynamics of the transition region. *NewAR* **44**, 599. DOI. ADS.
- Gontikakis, C., Peter, H., Dara, H.C.: 2003, Sizes of quiet Sun transition region structures. *A&A* **408**, 743. DOI. ADS.
- Guerreiro, N., Hansteen, V., De Pontieu, B.: 2013, The Cycling of Material between the Solar Corona and Chromosphere. *ApJ* **769**, 47. DOI. ADS.
- Hansteen, V., De Pontieu, B., Carlsson, M., Lemen, J., Title, A., Boerner, P., Hurlburt, N., Tarbell, T.D., Wuelser, J.P., Pereira, T.M.D., De Luca, E.E., Golub, L., McKillop, S., Reeves, K., Saar, S., Testa, P., Tian, H., Kankelborg, C., Jaeggli, S., Kleint, L., Martínez-Sykora, J.: 2014, The unresolved fine structure resolved: IRIS observations of the solar transition region. *Science* **346**, 1255757. DOI. ADS.
- Harrison, R.A.: 1997, EUV Blinkers: The Significance of Variations in the Extreme Ultraviolet Quiet Sun. *Sol. Phys.* **175**, 467. DOI. ADS.
- Henriques, V.M.J., Kuridze, D., Mathioudakis, M., Keenan, F.P.: 2016, Quiet-Sun H α Transients and Corresponding Small-scale Transition Region and Coronal Heating. *ApJ* **820**, 124. DOI. ADS.
- Judge, P.G., Pietarila, A.: 2004, On the Formation of Extreme-Ultraviolet Helium Lines in the Sun: Analysis of SOHO Data. *ApJ* **606**, 1258. DOI. ADS.
- Kayshap, P., Banerjee, D., Srivastava, A.K.: 2015, Diagnostics of a Coronal Hole and the Adjacent Quiet Sun by The Hinode/EUV Imaging Spectrometer (EIS). *Sol. Phys.* **290**, 2889. DOI. ADS.
- Klimchuk, J.A.: 2012, The role of type II spicules in the upper solar atmosphere. *Journal of Geophysical Research (Space Physics)* **117**, A12102. DOI. ADS.
- Klimchuk, J.A., Bradshaw, S.J.: 2014, Are Chromospheric Nanoflares a Primary Source of Coronal Plasma? *ApJ* **791**, 60. DOI. ADS.
- Kontogiannis, I., Tsiropoula, G., Tziotziou, K.: 2011, Hinode SOT/SP and SoHO/MDI quiet Sun magnetic field. Implications of their differences on the extrapolated chromospheric field and the height of the magnetic canopy. *A&A* **531**, A66. DOI. ADS.

- Kontogiannis, I., Tsiropoula, G., Tziotziou, K., Georgoulis, M.K.: 2010, Oscillations in a network region observed in the H α line and their relation to the magnetic field. *A&A* **524**, A12. DOI. ADS.
- Leenaarts, J., Rutten, R.J., Sütterlin, P., Carlsson, M., Uitenbroek, H.: 2006, DOT tomography of the solar atmosphere. VI. Magnetic elements as bright points in the blue wing of H α . *A&A* **449**, 1209. DOI. ADS.
- Levens, P.J., Labrosse, N., Fletcher, L., Schmieder, B.: 2015, A solar tornado observed by EIS. Plasma diagnostics. *A&A* **582**, A27. DOI. ADS.
- Lites, B.W., Kubo, M., Socas-Navarro, H., Berger, T., Frank, Z., Shine, R., Tarbell, T., Title, A., Ichimoto, K., Katsukawa, Y., Tsuneta, S., Suematsu, Y., Shimizu, T., Nagata, S.: 2008, The Horizontal Magnetic Flux of the Quiet-Sun Internetwork as Observed with the Hinode Spectro-Polarimeter. *ApJ* **672**, 1237. DOI. ADS.
- MacPherson, K.P., Jordan, C.: 1999, The anomalous intensities of helium lines in the quiet solar transition region. *MNRAS* **308**, 510. DOI. ADS.
- Madjarska, M.S., Doyle, J.G.: 2003, Simultaneous observations of solar transition region blinkers and explosive events by SUMER, CDS and BBSO. Are blinkers, explosive events and spicules the same phenomenon? *A&A* **403**, 731. DOI. ADS.
- Madjarska, M.S., Doyle, J.G., Hochedez, J.-F., Theissen, A.: 2006, Macrospicules and blinkers as seen in Shutterless EIT 304 Å. *A&A* **452**, L11. DOI. ADS.
- McIntosh, S.W., De Pontieu, B.: 2009a, High-Speed Transition Region and Coronal Upflows in the Quiet Sun. *ApJ* **707**, 524. DOI. ADS.
- McIntosh, S.W., De Pontieu, B.: 2009b, Observing Episodic Coronal Heating Events Rooted in Chromospheric Activity. *ApJ Lett.* **706**, L80. DOI. ADS.
- Nelson, C.J., Doyle, J.G.: 2013, Excitation of an outflow from the lower solar atmosphere and a co-temporal EUV transient brightening. *A&A* **560**, A31. DOI. ADS.
- Patsourakos, S., Gouttebroze, P., Vourlidas, A.: 2007, The Quiet Sun Network at Subarcsecond Resolution: VAULT Observations and Radiative Transfer Modeling of Cool Loops. *ApJ* **664**, 1214. DOI. ADS.
- Pereira, T.M.D., De Pontieu, B., Carlsson, M., Hansteen, V., Tarbell, T.D., Lemen, J., Title, A., Boerner, P., Hurlburt, N., Wülser, J.P., Martínez-Sykora, J., Kleint, L., Golub, L., McKillop, S., Reeves, K.K., Saar, S., Testa, P., Tian, H., Jaeggli, S., Kankelborg, C.: 2014, An Interface Region Imaging Spectrograph First View on Solar Spicules. *ApJ Lett.* **792**, L15. DOI. ADS.
- Peter, H.: 2001, On the nature of the transition region from the chromosphere to the corona of the Sun. *A&A* **374**, 1108. DOI. ADS.
- Peter, H., Judge, P.G.: 1999, On the Doppler Shifts of Solar Ultraviolet Emission Lines. *ApJ* **522**, 1148. DOI. ADS.
- Roupe van der Voort, L., Leenaarts, J., de Pontieu, B., Carlsson, M., Vissers, G.: 2009, On-disk Counterparts of Type II Spicules in the Ca II 854.2 nm and H α Lines. *ApJ* **705**, 272. DOI. ADS.
- Roupe van der Voort, L., De Pontieu, B., Pereira, T.M.D., Carlsson, M., Hansteen, V.: 2015, Heating Signatures in the Disk Counterparts of Solar Spicules in Interface Region Imaging Spectrograph Observations. *ApJ Lett.* **799**, L3. DOI. ADS.
- Rutten, R.J., Hammerschlag, R.H., Bettonvil, F.C.M., Sütterlin, P., de Wijn, A.G.: 2004, DOT tomography of the solar atmosphere. I. Telescope summary and program definition. *A&A* **413**, 1183. DOI. ADS.
- Sasso, C., Andretta, V., Spadaro, D.: 2015, Modelling low-lying, cool solar loops with optically thick radiative losses. *A&A* **583**, A54. DOI. ADS.
- Sasso, C., Andretta, V., Spadaro, D., Susino, R.: 2012, Solar low-lying cool loops and their contribution to the transition region EUV output. *A&A* **537**, A150. DOI. ADS.
- Scherrer, P.H., Bogart, R.S., Bush, R.I., Hoeksema, J.T., Kosovichev, A.G., Schou, J., Rosenberg, W., Springer, L., Tarbell, T.D., Title, A., Wolfson, C.J., Zayer, I., MDI Engineering Team: 1995, The Solar Oscillations Investigation - Michelson Doppler Imager. *Sol. Phys.* **162**, 129. DOI. ADS.
- Schmidt, H.U.: 1964, On the Observable Effects of Magnetic Energy Storage and Release Connected With Solar Flares. *NASA Special Publication* **50**, 107. ADS.
- Schmit, D.J., De Pontieu, B.: 2016, What Is the Source of Quiet Sun Transition Region Emission? *ApJ* **831**, 158. DOI. ADS.
- Schrijver, C.J., Title, A.M.: 2003, The Magnetic Connection between the Solar Photosphere and the Corona. *ApJ Lett.* **597**, L165. DOI. ADS.

- Schrijver, C.J., Title, A.M., van Ballegoijen, A.A., Hagenaar, H.J., Shine, R.A.: 1997, Sustaining the Quiet Photospheric Network: The Balance of Flux Emergence, Fragmentation, Merging, and Cancellation. *ApJ* **487**, 424. ADS.
- Tian, H., Tu, C.-Y., Xia, L.-D., He, J.-S.: 2008a, Radiance and Doppler shift distributions across the network of the quiet Sun. *A&A* **489**, 1297. DOI. ADS.
- Tian, H., Marsch, E., Tu, C.-Y., Xia, L.-D., He, J.-S.: 2008b, Sizes of transition-region structures in coronal holes and in the quiet Sun. *A&A* **482**, 267. DOI. ADS.
- Tian, H., Marsch, E., Tu, C., Curdt, W., He, J.: 2010, New views on the emission and structure of the solar transition region. *NewAR* **54**, 13. DOI. ADS.
- Tian, H., DeLuca, E.E., Cranmer, S.R., De Pontieu, B., Peter, H., Martínez-Sykora, J., Golub, L., McKillop, S., Reeves, K.K., Miralles, M.P., McCauley, P., Saar, S., Testa, P., Weber, M., Murphy, N., Lemen, J., Title, A., Boerner, P., Hurlburt, N., Tarbell, T.D., Wuelser, J.P., Kleint, L., Kankelborg, C., Jaeggli, S., Carlsson, M., Hansteen, V., McIntosh, S.W.: 2014, Prevalence of small-scale jets from the networks of the solar transition region and chromosphere. *Science* **346**(27), 1255711. DOI. ADS.
- Tsiropoula, G.: 2000, Determination of the line-of-sight velocities in the dark penumbral fibrils. *NewAR* **5**, 1. DOI. ADS.
- Tsiropoula, G., Tziotziou, K.: 2004, The role of chromospheric mottles in the mass balance and heating of the solar atmosphere. *A&A* **424**, 279. DOI. ADS.
- Tsiropoula, G., Tziotziou, K., Kontogiannis, I., Madjarska, M.S., Doyle, J.G., Suematsu, Y.: 2012, Solar Fine-Scale Structures. I. Spicules and Other Small-Scale, Jet-Like Events at the Chromospheric Level: Observations and Physical Parameters. *Space Sci. Rev.* **169**, 181. DOI. ADS.
- Tsuneta, S., Ichimoto, K., Katsukawa, Y., Nagata, S., Otsubo, M., Shimizu, T., Suematsu, Y., Nakagiri, M., Noguchi, M., Tarbell, T., Title, A., Shine, R., Rosenberg, W., Hoffmann, C., Jurcevich, B., Kushner, G., Levay, M., Lites, B., Elmore, D., Matsushita, T., Kawaguchi, N., Saito, H., Mikami, I., Hill, L.D., Owens, J.K.: 2008, The Solar Optical Telescope for the Hinode Mission: An Overview. *Sol. Phys.* **249**, 167. DOI. ADS.
- Ugarte-Urra, I., Doyle, J.G., Nakariakov, V.M., Foley, C.R.: 2004, CDS wide slit time-series of EUV coronal bright points. *A&A* **425**, 1083. DOI. ADS.
- Vourlidas, A., Sanchez Andrade-Nuño, B., Landi, E., Patsourakos, S., Teriaca, L., Schühle, U., Korendyke, C.M., Nestoras, I.: 2010, The Structure and Dynamics of the Upper Chromosphere and Lower Transition Region as Revealed by the Subarcsecond VAULT Observations. *Sol. Phys.* **261**, 53. DOI. ADS.
- Young, P.R., Del Zanna, G., Mason, H.E., Dere, K.P., Landi, E., Landini, M., Doschek, G.A., Brown, C.M., Culhane, L., Harra, L.K., Watanabe, T., Hara, H.: 2007, EUV Emission Lines and Diagnostics Observed with Hinode/EIS. *PASJ* **59**, S857. DOI. ADS.